
Article:
Ede, J.D., Zhu, Z.Q. and Howe, D. (2002) Rotor resonances of high-speed permanent-magnet brushless machines. IEEE Transactions on Industry Applications, 38 (6). pp. 1542-1548. ISSN 0093-9994

https://doi.org/10.1109/TIA.2002.804765

Rotor Resonances of High-Speed Permanent-Magnet Brushless Machines

Jason D. Ede, Z. Q. Zhu, *Senior Member, IEEE*, and David Howe

***Abstract*—For high-speed machines, in particular, it is very important to accurately predict natural frequencies of the rotor at the design stage so as to minimize the likelihood of failure. Finite-element analysis and experimental measurements are used to establish the natural frequencies and modes of the rotor of a high-speed permanent-magnet brushless motor, and to assess the influence of leading design parameters, such as the active length, the shaft diameter and extension, the bearings, and the material properties.**

***Index Terms*—Brushless motor, high speed, mechanical resonance, permanent-magnet machine, vibration.**

I. Introduction

PERMANENT-MAGNET brushless motors having rotational speeds of around 100 kr/min are emerging as a key technology, due to their high efficiency, high power density, and low weight [1]–[5]. They are being employed in applications such as compressors, centrifuges, and vacuum pumps, and a variety of different issues have been investigated. In [1], Takahashi *et al.* constructed and tested a 5-kW motor operating at 150 000 r/min using a sensorless commutation strategy. A different sensorless strategy was applied in [2], where a motor and control strategy were employed to facilitate operation at speeds up to 60 000 r/min. In [3], the influence of the rotor to stator diameter on a two-pole brushless dc motor operating at 20 000 r/min was investigated. However, in all of these papers, the effect of rotor resonances has been either neglected or not mentioned. In [4], the rotor resonance is taken into account, but only with regard to the whirl speed of the rotor as much as it affects the air journal bearings which were used. Similarly, high-speed permanent-magnet brushless generators are being employed in applications such as gas-turbine-driven generators (CHP) and electric/hybrid vehicle traction systems [5]. However, due to their high fundamental frequency, careful consideration needs to be given to both electromagnetic and mechanical design issues.

Accurate prediction of the natural frequencies and modes of the rotor at the design stage is clearly critical, since an inappropriate rotor design may lead to excessive acoustic noise emissions, excessive bearing loss, and even catastrophic failure. By way of example, Fig. 1 shows one of our early prototype motors, which exhibited a rotor resonance at $\approx$ 100 000 r/min, causing the rotor shaft to bend and consequently damage the end-caps and bearings.

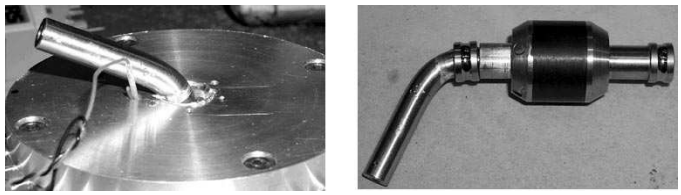

Fig. 1. Catastrophic failure of rotor due to resonance.

However, apart from a few notable textbooks [6], [7] and papers on issues related to rotor resonances, e.g., behavior of laminated stacks [8]–[10] and unsymmetrical shafts [11], little systematic work has been carried out on this aspect in recent years.

This paper describes the finite-element analysis (FEA) of the rotor of a permanent magnet brushless dc motor having a rated speed and power of 120 000 r/min and 1.25 kW, respectively, and investigates the influence of design parameters, such as the axial length, the shaft length and diameter, on the natural frequencies. FEA predictions, using the ANSYS FE package, are validated extensively by measurements from impulse force response tests, using a modal impulse force hammer, an accelerometer, and a dynamic signal analyzer, HP 35660A. While the addition of a stator will affect the resonance modes, due to the interaction of the rotor permanent magnets with the stator, this is neglected in order to simplify the study. However, this will not affect the general observations. The main focus in this paper is on the resonant modes that will be excited during normal operation. Primarily, this includes all modes below the operating speed of the motor (2 kHz), but it is appreciated that the commutation strategy may excite resonance modes above 2 kHz, although that is not considered within this paper. The paper also considers the influence of the bearings and various design parameters on the motor performance.

II. Influence of Rotor Design

The rotor, shown in Fig. 2, consists of a steel shaft with an integral end-cap at one end, and the other end-cap being pinned in place after the laminations have been inserted on the shaft. The permanent magnets are bonded to the laminations with a high-strength adhesive, and contained within a carbon-fiber/ epoxy

Paper IPCSD 02–053, presented at the 2001 IEEE International Electric Machines and Drives Conference, Cambridge, MA, June 17–20, and approved for publication in the IEEE TRANSACTIONS ON INDUSTRY APPLICATIONS by the Electric Machines Committee of the IEEE Industry Applications Society. Manuscript submitted for review March 17, 2001 and released for publication July 24, 2002.

The authors are with the Department of Electronic and Electrical Engineering, University of Sheffield, Sheffield S1 3JD, U.K. (e-mail: j.ede@shef.ac.uk; z.q.zhu@shef.ac.uk; d.howe@shef.ac.uk).

Digital Object Identifier 10.1109/TIA.2002.804765

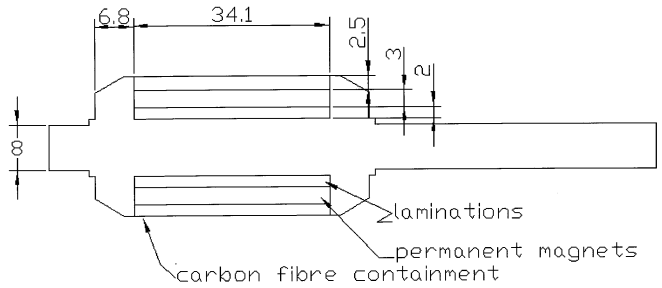

Fig. 2. Schematic of rotor.

TABLE I
NATURAL FREQUENCIES FOR CIRCULAR SHAFT

Mode	Analytical (Hz)	Finite element (Hz)	Measured (Hz)
1st bending	3046	3047	2944
2nd bending	8542	8226	8256
Rotational	-	14727	-
3rd bending	16752	15683	15168

over-wrap. The rotor shaft was machined from AISI 303, a non-magnetic stainless steel. The properties of the various materials are given in the Appendix.

Initially, a circular steel shaft, machined from AISI 303, was considered. It had a diameter of 7.9 mm and an axial length of 106 mm. The shaft natural frequencies may be calculated analytically from [6]

$$\omega_n = a_n \sqrt{\frac{EI}{\mu_1 l^4}} \tag{1}$$

where E, I, μ_1, and I are the Young's modulus, inertia, mass per unit length, and length of the shaft, respectively, and a_n is a numerical constant calculated by the Rayleigh method, which is dependent on the problem boundaries. From [6], the values of a_n for the first three free bending modes are: $a_1 = 22$, $a_2 = 61.7$, and $a_3 = 121$. Table I compares the FE and analytically calculated natural frequencies, with measurements, while Fig. 3 shows the vibration mode shapes. As can be seen, the predicted values agree well with the measurements.

The rotor shaft with an integral end-cap, as shown in Fig. 4, was then considered. As can be seen, a flat surface was machined on to each side of the shaft in order to locate the laminations since a keyway would lead to an undesirable imbalance. Although this was not included in the FE model, it can lead to dual peaks at the vibration modes, which can show up on the measured vibration frequency spectrum, [11].

FE predictions of the natural frequencies agree well with the measured values, as can be seen from the frequency spectrum of Fig. 5 and Table II. It will be noted that the rotational vibration mode was not excited by the measurement, and that natural frequencies for the rotor shaft are slightly higher than for the simple circular shaft due to the larger diameter and, hence, increased stiffness, of the active section. This increase would have been greater without the end-cap, which increases the mass and thereby reduces the natural frequency.

The silicon iron rotor laminations are held under compressive force by a second end-cap, as seen in Fig. 6. The effective properties of such lamination stacks have been characterized previously by the authors in [8], while [9] reported that the axial component of Young's modulus for laminated cores can be as low as 0.25% of the value for the solid material, and depends on the clamping pressure. Since it is difficult to determine effective properties of a particular lamination stack, material properties which were used on the three–dimensional (3-D) FEA were

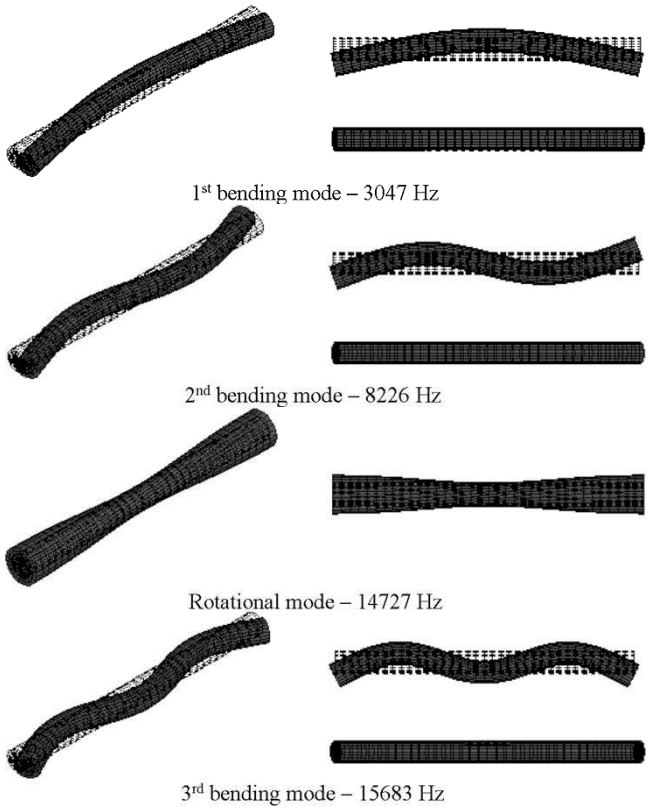

Fig. 3. Vibration modes for a steel bar.

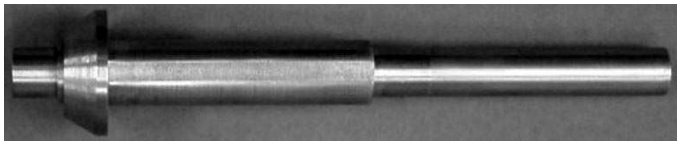

Fig. 4. Rotor shaft/end-cap.

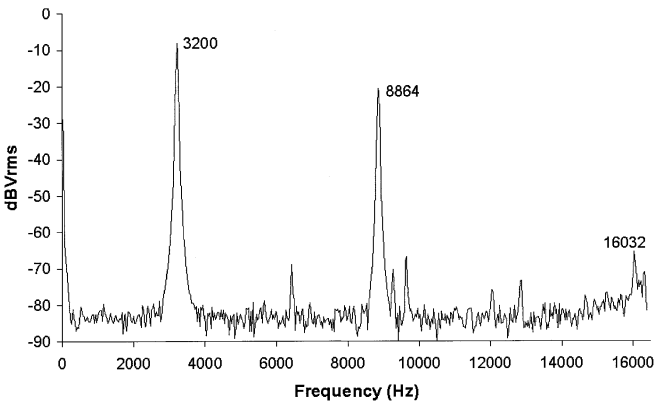

Fig. 5. Frequency spectrum for rotor shaft/end-cap.

TABLE II
NATURAL FREQUENCIES OF ROTOR SHAFT/END-CAP

Mode	Finite element (Hz)	Measured (Hz)
1st bending	3138	3200
2nd bending	8751	8864
Rotational	11710	-
3rd bending	15906	16032

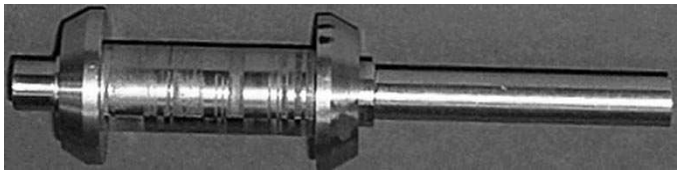

Fig. 6. Rotor shaft, laminations, and end-caps.

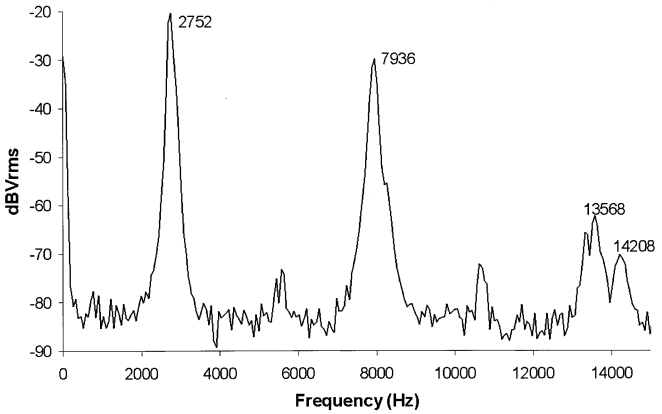

Fig. 7. Frequency spectrum for shaft with laminations and end-cap.

TABLE III
NATURAL FREQUENCIES OF ROTOR SHAFT WITH LAMINATIONS AND END-CAPS

Mode	Finite element (Hz)	Measured (Hz)
1st bending	2766	2752
2nd bending	7941	7936
Rotational	8806	-
3rd bending	14082	13568

varied until predicted frequency response of the rotor compared well with the measured response.

The deduced material properties for the rotor laminations are given in the Appendix, while the measured natural frequency spectrum is shown in Fig. 7. Table III compares FE predicted natural frequencies with measured values. As can be seen, the natural frequencies are significantly lower than those shown in Table I, largely due to the addition of the second end-cap, which adds to the mass of the rotor without contributing to the axial stiffness. The laminations also serve to reduce the natural frequency, as they increase the mass and make little contribution to the axial stiffness.

The addition of the sintered NdFeB magnets which have a comparatively high Young's modulus significantly increases the axial stiffness of the rotor, and thereby causes the natural frequencies to increase. The vibration frequency spectrum and the comparison of the measured and FE predicted natural frequencies are shown in Fig. 8 and Table IV, respectively.

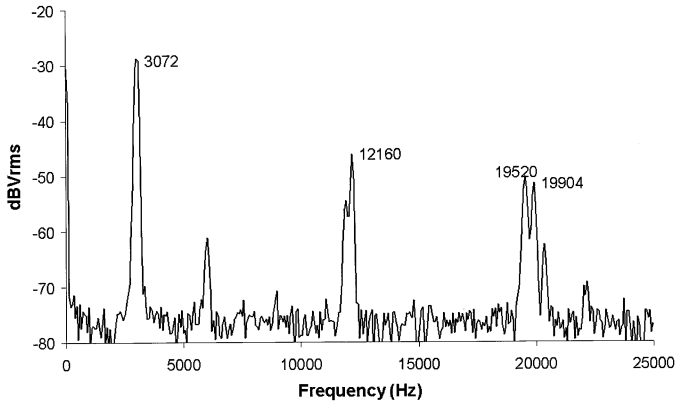

Fig. 8. Frequency spectrum for rotor shaft with laminations, end-caps, and magnets.

TABLE IV
NATURAL FREQUENCIES OF ROTOR SHAFT WITH LAMINATIONS, END-CAPS, AND MAGNETS

Mode	Finite element (Hz)	Measured (Hz)
1st bending	3052	3008
2nd bending	12609	12160
Rotational	15410	-
3rd bending	21201	19904

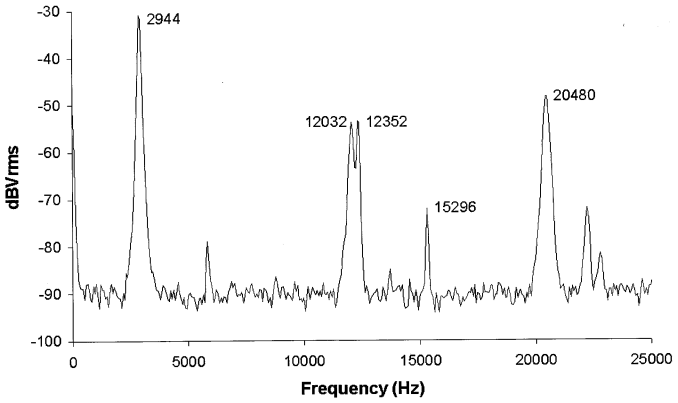

Fig. 9. Frequency spectrum of assembled rotor.

The addition of the 2-mm-thick carbon-fiber containment, had little effect on the natural frequencies, since it is a relatively lightweight material. The stiffness of the carbon-fiber containment in the axial direction is very low, while its Young's modulus in the circumferential direction is comparable to that for mild steel. The vibration frequency spectrum for the fully assembled rotor is shown in Fig. 9, while Table V compares predicted and measured natural frequencies from those predicted by FEA. The corresponding rotor vibrational modes are shown in Fig. 10.

In summary, the rotor natural frequencies can be accurately predicted by FEA, while various rotor components have significant influence on the natural frequencies and modes of the

TABLE V
NATURAL FREQUENCIES OF ASSEMBLED ROTOR

Mode	Finite element (Hz)	Measured (Hz)
1st bending	3026	2944
2nd bending	12641	12352
Rotational	15421	15296
3rd bending	21504	20480

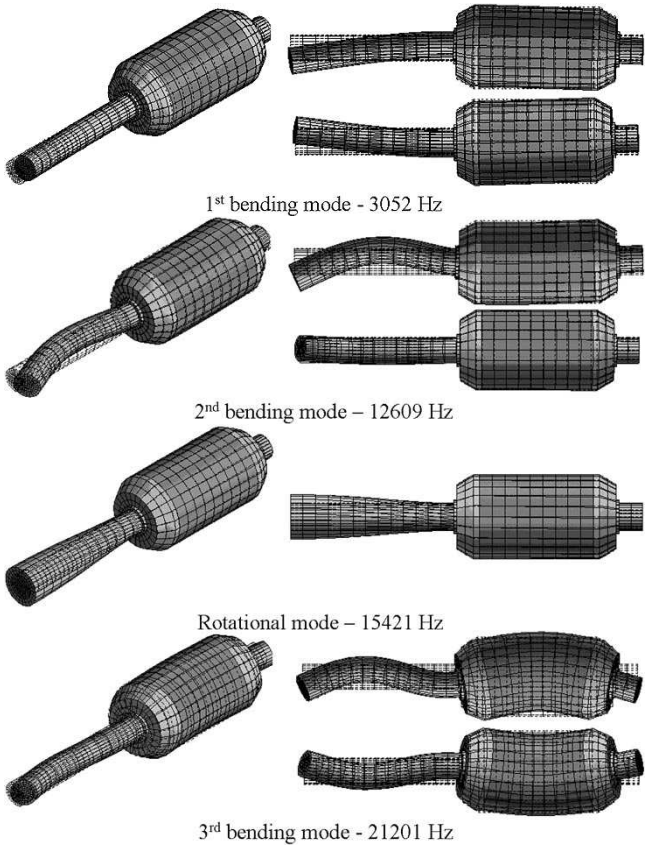

Fig. 10. Vibration modes for completed rotor.

rotor. It has also been shown that the addition of the laminations, end-caps, and the carbon-fiber over-wrap decreases the natural frequencies of the rotor as they contribute mass to the shaft, but very little axial stiffness, while the addition of the magnets increases the axial stiffness of the rotor shaft and, hence, increases the natural frequencies significantly.

III. INFLUENCE OF BEARINGS

The mounting of the rotor in bearings not only changes the vibration modes slightly, but also introduces two new vibrational modes, i.e., the cylindrical and conical modes. A detailed description of these modes is given in [7]. For a "rigid" rotor the frequency of the cylindrical mode is $\omega = \sqrt{(2K/m)}$ where K is the bearing stiffness, or spring constant, and m is the rotor mass, and this can often lie within the operating speed range.

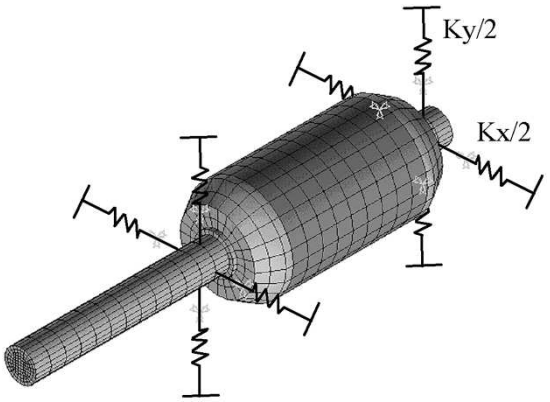

Fig. 11. FE model of rotor with bearings.

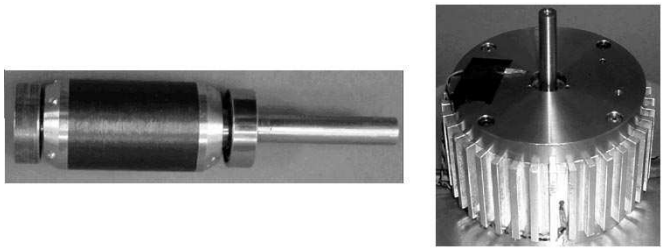

Fig. 12. Rotor and bearings, and assembled motor.

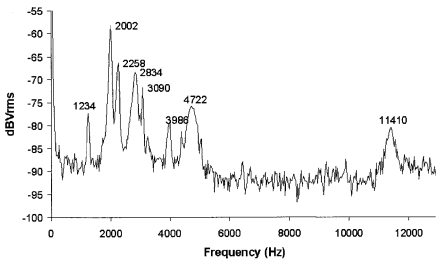

Frequency (Hz)	Mode source
1234	Frame
2002	**Rotor**
2258	Frame
2834	**Rotor**
3090	Frame
3986	**Rotor**
4722	**Rotor**
11410	**Rotor**

Fig. 13. Frequency spectrum for assembled motor and likely origin of resonances.

However, in practice, the rotor is flexible, which necessitates FEA to accurately model the rotor and bearings. Ceramic ball bearings specially designed for high-speed operation were employed in the motor under consideration.

In the FEA, the bearings were modeled as springs, four springs being used for each bearing to ensure that the rotor shaft is supported evenly, as can be seen in the FE mesh shown in Fig. 11, the actual rotor and bearing system together with the assembled motor being shown in Fig. 12.

The natural frequencies of the frame were determined experimentally, but are not shown due to space limitations. The measured vibration spectrum of the rotor when mounted in its bearings in the assembled motor is shown in Fig. 13, together with the probable origin of each of the natural frequencies.

The bearing stiffness was determined by varying the bearing stiffness in the FE model until the curves shown in Fig. 14,

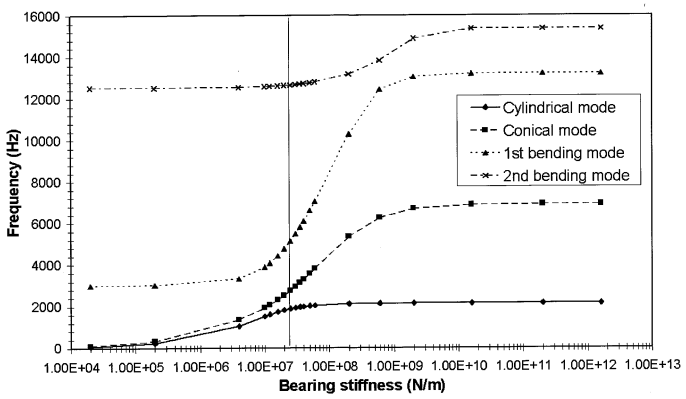

Fig. 14. Derivation of bearing stiffness.

TABLE VI
NATURAL FREQUENCIES FOR ROTOR

Mode	Finite element (Hz)	Measured (Hz)
Cylindrical	1892	2002
Conical	2748	2834
1st bending	5140	4722
2nd bending	12662	11410

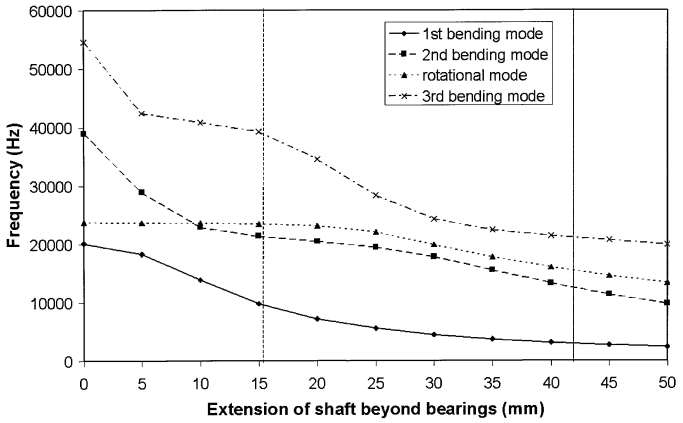

Fig. 15. Effect of shaft extension on natural frequencies.

were obtained. The bearing stiffness which was deduced to be $2.5 * 10^7$ N/m, which compares with a nominal stiffness of $\sim 5 * 10^7$ N/m for ceramic ball bearings.

As can be seen from Table VI, the measured and predicted natural frequencies of the rotor compare well, the difference being caused by the influence of the motor frame and the pre-load on the bearings.

IV. INFLUENCE OF DESIGN PARAMETERS

The axial length of the shaft can have a significant effect on the rotor natural frequencies, as shown in Fig. 15, in which the solid line corresponds to the rotor which was described earlier and had a 42-mm shaft extension, and the dotted line which corresponds to another rotor with a 15-mm shaft extension, and by comparing Fig. 16 with Fig. 9 and Table VII with Table V. By shortening the shaft, the frequency of the first vibration mode increases from 3 to almost 10 kHz.

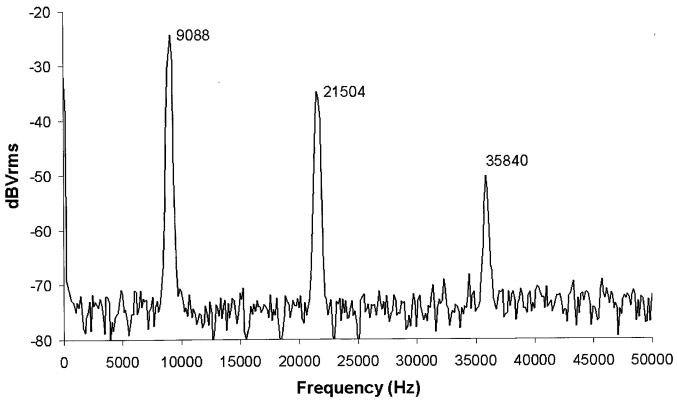

Fig. 16. Frequency spectrum for rotor with 15-mm shaft extension.

TABLE VII
NATURAL FREQUENCIES OF ROTOR WITH 15-MM EXTENSION

Mode	Finite element (Hz)	Measured (Hz)
1st bending	9816	9088
2nd bending	21374	21504
Rotational	23477	-
3rd bending	39339	35840

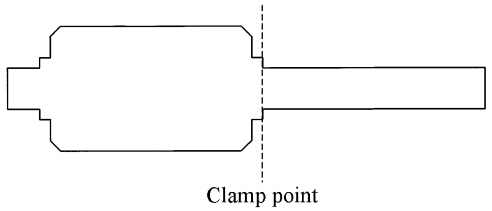

Fig. 17. Rotor with shaft extension.

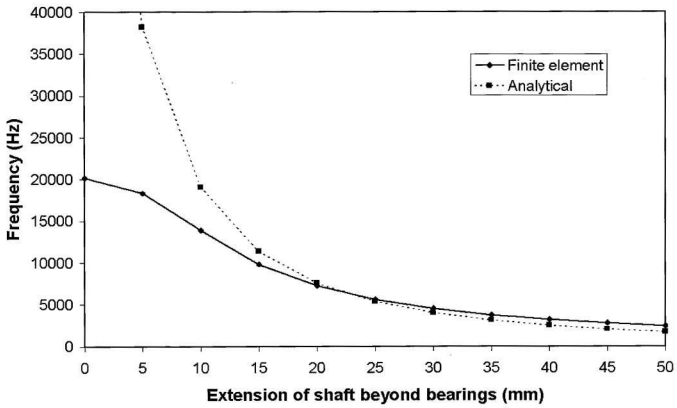

Fig. 18. Variation of frequency of first bending mode with shaft extension.

The shaft extension can be viewed as a clamped beam, as shown in Fig. 17, the natural frequencies which are again given by (1), in which a_n is now given as 3.52 [6] for the first bending mode. Fig. 18 compares the analytically calculated and FE-calculated frequency of the first bending mode. When the shaft extension is reduced below 15 mm, this vibration mode is dominated by flexing of the active section of the rotor, which effectively imposes an upper limit on the natural frequency which results from reducing the shaft extension.

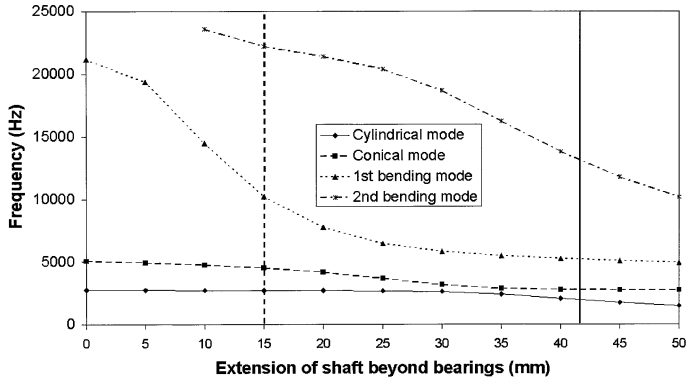

Fig. 19. Effect of shaft extension on natural frequencies (with bearings).

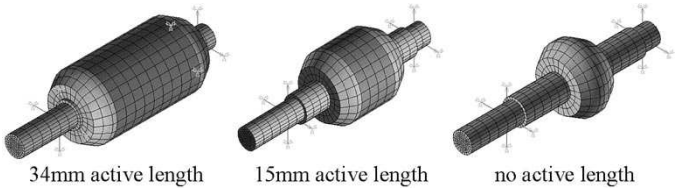

Fig. 20. Reduction in active length.

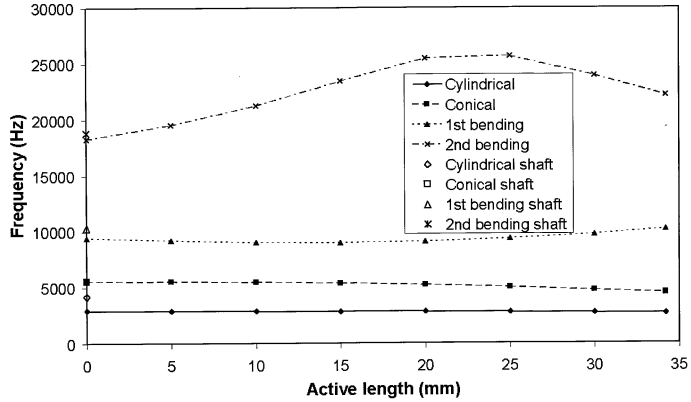

Fig. 21. Variation of natural frequencies with active length with bearings.

By incorporating the bearings into the model, the influence of the shaft extension on the bearing modes can be further investigated. It can be seen from Fig. 19 that, although the shaft length significantly affects the bending modes, the effect on the cylindrical and conical bearing modes is minimal. The bending modes follow the same pattern as shown previously in Fig. 15, with solid and dotted lines corresponding to 42- and 15-mm shaft extensions, respectively.

In the remaining analyses, the shaft extension was maintained at 15 mm in order to prevent it dominating the vibration mode shapes. The axial length of the active section of the rotor was then reduced as shown in Fig. 20. This makes the shaft lighter and, at the same time, reduces the stiffness of the central section of the rotor.

Fig. 21 shows the resulting variation of the natural frequencies of the bearing modes and the first two bending modes. The natural frequency of the bearing modes gradually increases as the rotor mass is reduced, as expected.

The frequency of the first bending mode reduces slightly as the active length of the rotor is reduced and the rotor becomes more flexible. As regards the second bending mode, as the active length and, therefore, the rotor mass is decreased the natural frequency initially increases. However, when the active length is reduced below 20 mm, the shaft starts to flex and the natural frequency of this mode decreases.

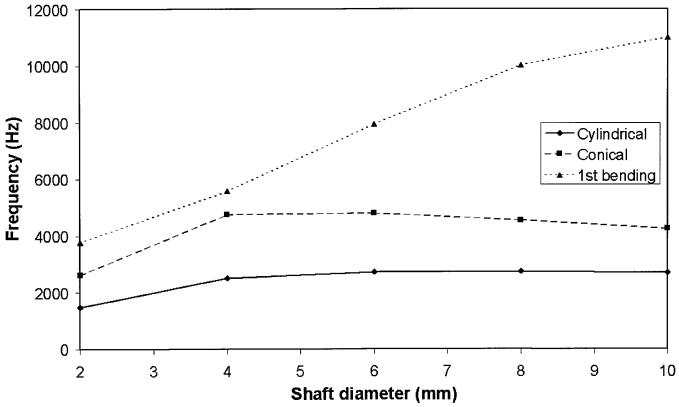

Fig. 22. Variation of natural frequencies with shaft diameter with bearings.

As regards the shaft diameter, a larger diameter provides greater axial strength and, hence, increases the natural frequencies of all the bending modes. However, the shaft diameter will ultimately be limited by the peripheral speed capability of the bearings.

Fig. 22 shows the effect of varying the shaft diameters from 2 to 10 mm on the natural frequencies of the bearing modes and the first bending mode, the active length of the rotor being 34.2 mm.

The second bending mode is not shown since it was not easily discernible. As will be seen, as the shaft diameter is reduced, initially there is a slight increase in the natural frequency of the cylindrical bearing mode due to the reduction in the weight of the shaft. However, as the shaft diameter is reduced further, the natural frequency reduces as the shaft begins to flex and dominate the mode shape. The variation of the natural frequency of the conical mode is somewhat similar. As will be seen, a reduction in the shaft diameter causes a significant reduction in the natural frequency of the first bending mode, as the shaft becomes more flexible. This can be clearly seen in the mode shapes of Fig. 23. With a shaft diameter of 10 mm, the characteristic mode shapes of the cylindrical and conical modes can clearly be observed. However, when the shaft diameter is reduced to 2 mm, deflection is due solely to the bending of the shaft.

V. Conclusions

FEA and experimental measurements have been used to investigate the influence of the rotor geometry on its natural frequencies. Where parameters were not available, effective values have been established by ensuring that FEAs agree with measurements. It is shown that the bearings introduce low-frequency cylindrical and conical vibration modes which often fall within the operating speed range of a motor. Investigations have also shown the influence of leading parameters on the rotor natural frequencies. It has been shown that the shaft extension has a significant influence on the natural frequencies, and in order to move rotor bending modes beyond the operating speed range the shaft should be short and have a large diameter.

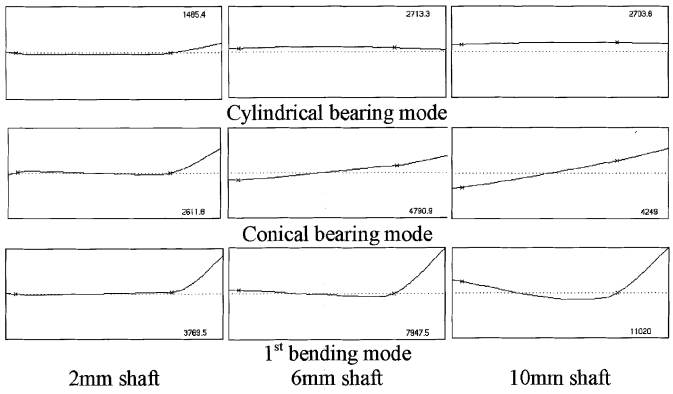

Fig. 23. Mode shapes for various shaft diameters with bearings.

TABLE VIII
STAINLESS STEEL (AISI 303)

Density (ρ)	8000 kg/m^3
Young's Modulus (E_x, E_y, E_z)	193 GPa
Shear modulus (G_{xy}, G_{xz}, G_{yz})	77.2 GPa
Poisson's ratio	0.3

TABLE IX
LAMINATIONS (M300-35A)

	Solid M300-35A	Laminated M300-35A
Density (ρ)	7650 kg/m^3	7305 kg/m^3
Young's modulus (E_x, E_y)	215 Gpa	215 GPa
Young's modulus (E_z)	215 Gpa	8 GPa
Shear modulus (G_{xy})	82.7 Gpa	55 GPa
Shear modulus (G_{xz}, G_{yz})	82.7 Gpa	8 GPa
Poisson's ratio (v_{xy})	0.3	0.3
Poisson's ratio (v_{yz}, v_{xz})	0.3	0.1

TABLE X
SINTERED NdFeB MAGNETS (UGIMAX 34B)

Density (ρ)	7500 kg/m^3
Young's Modulus (E_x, E_y, E_z)	160 GPa
Shear modulus (G_{xy}, G_{xz}, G_{yz})	61 GPa
Poisson's ratio	0.3

TABLE XI
CARBON FIBER/EPOXY COMPOSITE

Density (ρ)	1612.3 kg/m^3
Young's Modulus (E_r, E_z)	7.9 GPa
Young's Modulus (E_θ)	197 GPa
Shear modulus ($G_{r\theta}$, G_{rz}, $G_{\theta z}$)	6 GPa
Poisson's ratio ($v_{r\theta}$, v_{rz})	0.3
Poisson's ratio ($v_{\theta z}$)	0.0155

APPENDIX
MATERIAL PROPERTIES

See Tables VIII–XI.

REFERENCES

[1] I. Takahashi, T. Koganezawa, and K. Ohyama, "A super high speed PM motor drive system by a quasicurrent source inverter," *IEEE Trans. Ind. Applicat.*, vol. 30, pp. 683–690, May/June 1994.

[2] L. Xu and C. Wang, "Implementation and experimental investigation of sensorless control schemes for PMSM in super-high variable speed operation," in *Conf. Rec. IEEE-IAS Annu. Meeting*, 1998, CD-ROM.

[3] Z. Q. Zhu, K. Ng, and D. Howe, "Design and analysis of high-speed brushless permanent magnet motors," in *Proc. IEE EMD'97*, 1997, pp. 381–385.

[4] I. E. D. Pickup, D. Tipping, D. E. Hesmondhalgh, and B. A. T. Al Zahawi, "A 250 000 rpm drilling spindle using a permanent magnet motor," in *Proc. ICEM'96*, 1996, pp. 337–342.

[5] A. A. Pride and P. R. Evison, "100 to 140 krpm PM motor/generators for EV applications," in *Proc. IEE Colloq. Electrical Machine Design for All-Electric and Hybrid Electric Vehicles*, 1999, pp. 6/1–6/5.

[6] D. Hartog, *Mechanical Vibrations*, 4th ed. New York: McGraw-Hill, 1956.

[7] J. M. Vance, *Rotor Dynamics of Turbo Machinery*. New York: Wiley, 1988.

[8] S. A. Long, Z. Q. Zhu, and D. Howe, "Vibrational behavior of switched reluctance motors," *Proc. IEE—Elect. Power Applicat.*, vol. 148, pp. 257–264, 2001.

[9] S. D. Garvey, "The vibrational behavior of laminated components in electrical machines," in *Proc. IEE EMD'89*, 1989, pp. 226–231.

[10] K. Williams, R. K. Signal, and S. P. Verna, "Vibrations of long and short laminated structures of electrical machines Part II—Results for long stators," *J. Sound Vib.*, vol. 129, pp. 15–29, 1989.

[11] H. D. Taylor and N. Y. Schenectady, "Critical speed behavior of unsymmetrical shafts," *J. Appl. Mech.*, pp. A-71–A-79, June 1940.

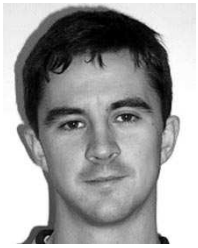

Jason D. Ede was born in Surrey, U.K., in 1974. He received the M.Eng. degree in 1997 from the University of Sheffield, Sheffield, U.K., where he is currently working toward the Ph.D. degree in high-speed permanent-magnet brushless dc motors in the Department of Electrical and Electronic Engineering.

He is also currently a Research Associate at the University of Sheffield, investigating fault-tolerant modular permanent-magnet motors.

Mr. Ede is an associate member of the Institution of Electrical Engineers, U.K.

Z. Q. Zhu (M'90–SM'00) received the B.Eng. and M.Sc. degrees from Zhejiang University, Hangzhou, China, in 1982 and 1984, respectively, and the Ph.D. degree from the University of Sheffield, Sheffield, U.K., in 1991, all in electrical and electronic engineering.

From 1984 to 1988, he lectured in the Department of Electrical Engineering, Zhejiang University. Since 1988, he has been with the University of Sheffield, where he is currently a Professor of Electronic and Electrical Engineering. His current major research interests include applications, control, and design of permanent-magnet machines and drives.

Prof. Zhu is a Chartered Engineer in the U.K. and a Member of the Institution of Electrical Engineers, U.K.

David Howe received the B.Tech. and M.Sc. degrees from the University of Bradford, Bradford, U.K., in 1966 and 1967, respectively, and the Ph.D. degree from the University of Southampton, Southampton, U.K., in 1974, all in electrical power engineering.

He has held academic posts at Brunel and Southampton Universities, and spent a period in industry with NEI Parsons Ltd., working on electromagnetic problems related to turbogenerators. He is currently a Professor of Electrical Engineering at the University of Sheffield, Sheffield, U.K., where he heads the Electrical Machines and Drives Research Group. His research activities span all facets of controlled electrical drive systems, with particular emphasis on permanent-magnet excited machines.

Prof. Howe is a Chartered Engineer in the U.K., and a Fellow of the Institution of Electrical Engineers, U.K.